Arab American University

Faculty of Graduate Studies

Structural and Optical Properties of $CdBr_2$ Films Deposited On to Ge Substrates

By

Lamiaa Mahmoud Fashafsha

Supervisor

Prof. Dr. Atef Fayez Qasrawi

This Thesis was submitted in partial fulfillment of the requirements for the Master's degree in Physics

October/2022

Structural and Optical Properties of $CdBr_2$ Films Deposited On to Ge Substrates

By

Lamiaa Mahmoud Fashafsha

This thesis was defended successfully on 13 October 2022 and approved by:

Committee members — Signature

1. Supervisor: Prof. Dr. Atef Fayez Qasrawi ------------------
2. External examiner: Assoc. Prof. Dr. Iyad Saadeddin ------------------
3. Internal examiner: Prof. Dr. Hazem Khanfar H.K ------------------

Declaration

The work provided in this thesis, unless otherwise referenced, is the researcher's own work, and has not been submitted elsewhere for any other degree or qualification.

العمل المقدم في هذه الرسالة, ما لم تتم الاشارة الى غير ذلك, هو عمل الباحث الخاص ولم يتم تقديمه في اي مكان اخر للحصول على اي درجة او مؤهل اخر.

Student's Name: Lamiaa Mahmoud Fashafsha

Signature: لمياء فشافشة

Data: 20/1/2023

To My Parents & Husband

Acknowledgement

Praise be to God, first and foremost, who has enabled me to achieve my dream. I completed my master's thesis from my beloved university "Arab American University". I extend my sincere thanks to all faculty members. In particular, Prof. Dr. Atef Qasrawi gave me knowledge and advice that was the basis for the success of the thesis. I offer him a lot of gratitude and may God reward him with all the best. All thank and love to my family who supported me all the time. I express my gratitude to my beloved parents, their prayers and support were the secret of my success, thanks to my husband who supported me and was the source of my hope and will. I give them a lot of gratitude. Thank you to my wonderful friends that are distinguished for their friendship, loyalty and giving. Last but not least, a big thank you to everyone that helped make the work possible.

Abstract

Structural and Optical Properties of $CdBr_2$ Films Deposited On to Ge Substrates

In this thesis cadmium bromide ($CdBr_2$) thin are coated onto glass and amorphous germanium (Ge) thin film substrates. The constructed Ge/$CdBr_2$ bilayers are structurally and optically characterized. The X-ray diffraction analysis have shown that the Ge, $CdBr_2$ and Ge/$CdBr_2$ films, which are grown by the thermal evaporation techniques, are of amorphous and polycrystalline structures, respectively. Coating $CdBr_2$ onto Ge caused a decrease in crystallite size a companied with an increase in the lattice parameters, microstrain, stacking faults and defect density. Optically, remarkable redshift in the transmittance and reflectance spectra is observed upon coating $CdBr_2$ onto Ge, which is considered as a substrate for $CdBr_2$. The light absorbability in the visible and infrared ranges of light increased by more than 80 times allowing large scale of light absorption. It is also noted that the energy band gap is redshifted from 3.32 to 3.27 eV as a result of depositing $CdBr_2$ on to glass by amorphous Ge substrates. On the other hand, the dielectric spectra of Ge/$CdBr_2$ mostly followed that of Ge meaning that the dielectric constant values have increased significantly. In addition, employing Drude – Lorentz model to determine the optical conductivity parameters have shown that the drift mobility and plasmon frequency of $CdBr_2$ can be increased when deposited on to glass by Ge. The plasmon frequency remarkably increased reaching values of 12 GHz making the Ge/$CdBr_2$ interfaces promising for application in communication technology.

Table of Contents

List of Tables

List of Figures

List of Symbols

Symbol	Symbol Meaning
Ge	Germanium
$CdBr_2$	Cadmium Bromide
λ	Wavelength
D	Inter-planner distance
Θ	Bragg angle
N	Integer
Hkl	Miller indices
D	Crystallite size
β	Full width of the peak at half maximum (FWHM) measured in radians
ε	Lattice strain
δ	Dislocation density
SF %	Stacking faults
E_g	Energy band gap
A	Absorption coefficient
T	Transmittance

R	Reflectance
A	Absorbance
m_r	Reduced mass
E_o	The width of the band tails
$K(\lambda)$	Extinction coefficient
ε_r	The real part of the dielectric constant
ε_{im}	The imaginary part of the dielectric constant
ε_{eff}	The effective dielectric constant
$n(\lambda)$	The refractive index
m_o	The electron mass

Chapter One

Introduction

Layered crystals like $CdBr_2$ have several polytypes which show non-Centro symmetric groups that give important optical and electrical effects [1]. It reported that $CdBr_2$ is an important compound in many optoelectronics including high gate dielectrics applications [2]. In addition, $CdBr_2$ micro/Nano belts can be employed as photodetectors [3]. It reported that $CdBr_2$/Cu polymer nano-composites establishes photo stimulated linear electro optical effects [4]. It is mentioned that SiO_2 layers enhances the crystallinity of $CdBr_2$ [5]. Thus $CdBr_2/SiO_2$ heterojunctions can be used in the technology of thin film transistors [2]. In the same context, Germanium (Ge) is reported to have applications in electronics in optoelectronics [6] and in photovoltaic devices [5]. It find applications as switching delay of reconfigurable field effect transistor and is used to reduce power consumption [7]. As a heterojunction element, Ge/Si heterojunction tunnel field effect transistor appear to be attractive for enhancement the ON-current of the device by replacing Si in the source region of Ge [8] which have smaller band gap of 0.67 eV compared with Si (1.12 eV) [6]. Hence it is widely used in reducing the tunneling barrier height [8]. Also Ge has many desirable properties, such as high mobility and large absorption coefficient near the infrared region [6].

There are many physical preparation techniques used in preparation thin films. It mentioned that the epitaxial layers of $Si_{1-x}Ge_x$ alloy grown by molecular beam epitaxy using the electron beam evaporation of Si and the thermal evaporation technique of Ge [9]. Axial Si-Ge nanowire heterojunctions are reported to be produced by the vapor-liquid-solid growth method by use nano clusters of Au as catalysts [10]. Slow evaporation for aqueous solution of the $CdBr_2$ solutes in water to prepare $CdBr_2$-$CdBr_2$:

Cu nano-heterostructures The thickness was controlling by the growth process due to convert the optical path on the border crystallites without the crystal [11]. physical vapor deposition technique used for preparing $CdBr_2$ thin films [2]. It is also observed that insertion of SiO_2 layers between $CdBr_2$ and Au resulted in an increase in the crystallite sizes and a decrease in the defect density of $CdBr_2$ in Au/$CdBr_2$/SiO_2/Au heterojunction devices [5]. In that study, it was reported that $CdBr_2$/SiO_2 heterojunctions have an amorphous structure while $CdBr_2$ has a hexagonal structure. The electron affinities of $CdBr_2$ is found to be 3.27 eV and it is energy band gap equal to 3.32 eV [2]. In another study $CdBr_2$ energy band gap is found to be 3.2 eV [3].

On the other hand, germanium (Ge) has many electrical and optical properties in the near infrared (NIR) and mid infrared (MIR) ranges [12]. Cubic-Ge has an indirect band gap that cannot emit light efficiently. But for hexagonal-Ge the band-folding effect results in a direct band gap so we get efficient light emission from direct-band gap of alloys [13]. It shown that when Ge concentration increased in polycrystalline $Cu_2ZnSn_{1-x}Ge_xS_4$ (CZTGS), electrical resistivity and hole mobility were decreased and carrier concentration was increased gradually [14]. It observed that Germanium based Bio Field Effect Transistor (BIOFET) has higher conductance than Silicon based BIOFET so Ge offers the best conductivity than Si [15].

The features of Ge substrates which strongly attenuate the characteristics of the epilayer, motivated us to use it in enhancing the optical performance of $CdBr_2$. Thus, in this work we will evaporate cadmium bromide ($CdBr_2$) thin film over Ge thin film under vacuum pressure of 10^{-5} mbar by physical vapor deposition technique in order to design and characterize a heterojunction device. The grown Ge/$CdBr_2$ will be treated as microwave resonator suitable for 5G technology. The notch frequencies and the return loss as well as the voltage standing wave ratios will be the main guides for the applicability of the $CdBr_2$ as resonators suitable for 5G technology.

Chapter Two

Theoretical Background

2.1 The X-ray Diffraction

X-ray Diffraction is useful technique to identification the crystalline materials, particle sizes, strains, preferred orientations by the following laws [16].

2.1.1 Bragg's Law

Constructive interference of radiation incident on planes occurs when the path difference equals an integral number n of wavelengths λ.

Under constructive interference Bragg's law is determined as [17]:

$$2d\sin\theta = n\lambda \qquad (2.1)$$

Where, d is defining as the distance between two planes of atoms, that is measured by angstrom unit.

θ is the angle between the plane surface and the incident beam of X-ray.

n is an integer numbers refers to the order of the corresponding reflection.

λ is the wavelength of the incident beam which is 1.5405 Å.

The structural phases are calculated from the measured plane distances, for the hexagonal crystal system the following equations are used:

$$\frac{1}{d^2} = \frac{4(h^2+hk+k^2)}{3a^2} + \frac{l^2}{c^2} \qquad (2.2)$$

Where, h , k and l are the miler indices, a & c are the lattice constant along a and c axis respectively [18].

In general crystal structures have 14 Bravais lattices in three dimensions are shown in table 2.1 , These 14 Bravais lattices are classified to 7 lattice systems (depend on the parameters and the angles for each of them) which are called : Triclinic, Monoclinic, Orthorhombic, Tetragonal, Trigonal, Cubic, and Hexagonal). For example, triclinic Bravais lattice Triclinic has three unequal lattice parameters a_1, a_2 and a_3; and three different (non-90°) lattice angles $a_{12} \neq a_{23} \neq a_{31}$ as shown in the following table.

Table 2.1. The Bravais lattices in three dimensions. [19]

Bravais lattice	Parameters	Simple (P)	Volume centered (I)	Base centered (C)	Face centered (F)
Triclinic	$a_1 \neq a_2 \neq a_3$ $a_{12} \neq a_{23} \neq a_{31}$	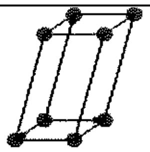			
Monoclinic	$a_1 \neq a_2 \neq a_3$ $a_{23} = a_{31} = 90^\circ$ $a_{12} \neq 90^\circ$	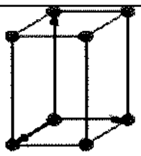	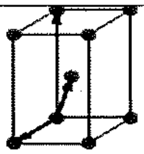		
Orthorhombic	$a_1 \neq a_2 \neq a_3$ $a_{12} = a_{23} = a_{31} = 90^\circ$	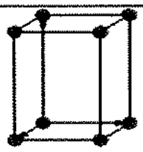	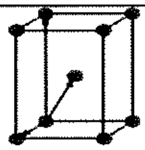	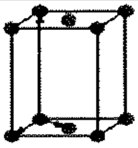	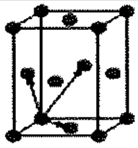
Tetragonal	$a_1 = a_2 \neq a_3$ $a_{12} = a_{23} = a_{31} = 90^\circ$	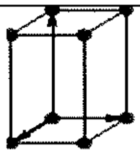	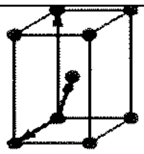		
Trigonal	$a_1 = a_2 = a_3$ $a_{12} = a_{23} = a_{31} < 120^\circ$	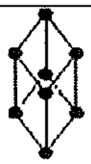			
Cubic	$a_1 = a_2 = a_3$ $a_{12} = a_{23} = a_{31} = 90^\circ$	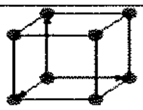	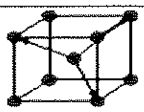		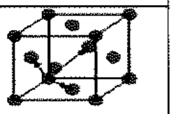
Hexagonal	$a_1 = a_2 \neq a_3$ $a_{12} = 120^\circ$ $a_{23} = a_{31} = 90^\circ$	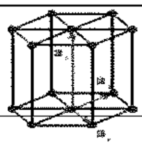			

2.1.2: Structural Parameters

Many structural parameters such as the Strain (ε), the crystallite size (D) and the Dislocation density (δ) determined from the broadening width β of the most X-ray diffraction peaks.

Strain (ε): is defining as the ratio of contraction in lengths of bonds to the lengths of main bonds' [18].

$$\varepsilon = \frac{\beta}{4\tan(\theta)} \tag{2.3}$$

"Crystallite" sizes(D) means the individual diameter "Crystallite" in the crystal [18].

$$D = \frac{0.94\lambda}{\beta\cos(\theta)} \tag{2.4}$$

Dislocation density (δ): is a measure of how many dislocations per unit volume of crystalline material [18], it is measured by (lines/cm^2) unit.

$$\delta = \frac{15\varepsilon}{aD} \tag{2.5}$$

Where, a is the lattice constant along a-axis .

Stacking faults (SF): is the defects which can happen in crystalline materials in two dimensional planar [18].

$$SF = \frac{2\pi^2}{45\sqrt{3\tan(\theta)}} \tag{2.6}$$

2.2 Optical Properties

The wide range of the optical properties of the semiconductor materials makes it very useful in optoelectronic applications.

2.2.1 Optical Processes Characterization

Ordinary classifications of optical processes include transmission, absorption and reflection. Consider a light beam has definite absorption thickness get in a medium from vacuum then, automatically the incident beam perhaps reflected from the front surface, or absorbent through until it arrived the back surface where it is possibly transmit or reflects outside the medium.

Refraction of light can be defined as light bending as it goes from an interface to another. Snell's law [20] described the bending of Light at two mediums interface.

$$n_1 \sin\theta_1 = n_2 \sin\theta_2 \tag{2.8}$$

In equation (2.8) the numbers indicate to the mediums.

2.2.2 Absorption of Light in Matter

Analysis of optical absorption spectrum is a good techniques to get information concerning to energy gap (E_g) and semiconductor materials band structure. Absorption is related with photon-electron interaction. When optical medium absorbs an incident photon, electron will transit from the valence to conduction band. The material light absorption is fixed via the absorption coefficient (α), that obvious the average of intensity attenuation over the propagated distance of incident light. Since the crystal momentum $\left(\frac{h}{a}\right)$ more than the photon momentum$\left(\frac{h}{\lambda}\right)$, when the photon is absorbed, electron momentum is maintained conservative. In situation of two parallel surfaces the transmittance of light is gained by the following formula [21],

$$T = (1 - R_1)e^{-\alpha d}(1 - R_2) \tag{2.9}$$

Where, $R_1$and R_2 indicate to the reflectivity's of the front and back surface of the film and d is thickness of the medium.

When, $R_1 = R_2$equation (2.9) becomes [18],

$$T = (1 - R_1)e^{-\alpha d} \tag{2.10}$$

The Absorption coefficient $\alpha(hv)$ is calculated from the following formula [22],

$$\alpha = \frac{-\ln(\frac{T}{(1-R_{glass})(1-R_{sample})}}{d} \tag{2.12}$$

2.2.3 Band Gap Calculations

The spectrophotometric absorption spectrum is used to determine the energy gap to achieve more information concerning to solids features. For this aim, Tauc's equation that joins between spectrophotometric absorption coefficient and the energy of incident photon, shows that energy bands gap is directly proportional to $((\alpha E)^{1/p}$. as shown in the following equation [23],

$$(\alpha E)^{1/p} = B(E - E_g) \tag{2.13}$$

Where,

E: The incident photon energy

p: An index which indicates to the type of the optical absorption process, it has the values 3, 3/2, 2 and 1/2 for indirect forbidden, direct forbidden, indirect allowed and direct allowed electronic transition respectively,

B : Constant, it depends on the electron transition probability.

E_g : The energy bands gap.

The E_g of the semiconductor material can be achieving from the intercept with E –axis of a graph of the $(\alpha E)^{1/p}$ versus the energy E of incident photon . The optical absorption processes graph selected shows a widest range of linier data in high absorption region.

2.2.4 Direct and Indirect Transitions

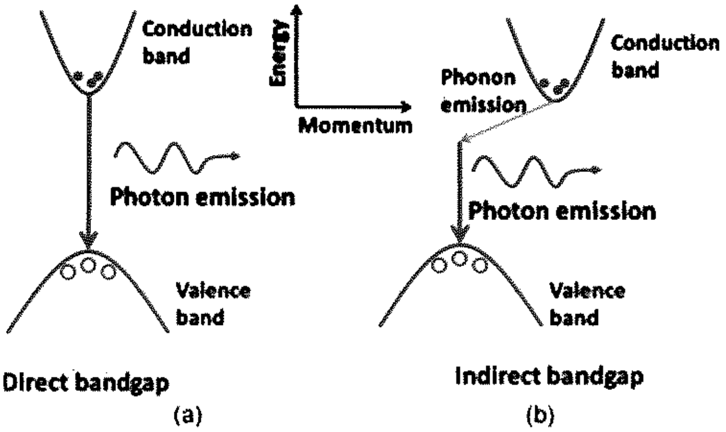

Fig.2.1. The (a) direct and (b) indirect semiconductor band gap transitions. [24]

Fig. 2.1 shows the (a) direct and (b) indirect band gap transition. For semiconductors, minimum and maximum states in conduction and valance bands respectively are distinguished by a certain momentum (k –vector) in the Brilouin zone. Fig. 2.1(a) shows the allowed direct absorption transition which assigned to the same momentum values for the bottom of the conduction band and the top of the valence band [25]. While the indirect band gap which is shown in Fig. 2.1 (b) assigned to a different k values for the bottom of the conduction band and the top of the valence band [25]. There is a phonon emission is shown in Fig. 2.1 (b) where phonons are either emitted or absorbed to complete transition from valence to the conduction band for an indirect electron.

2.2.5 Band Tails

The absorption coefficient gives enormous physical information. From the $\alpha - E$ spectra, the absorption saturation occurs when α displays constant variation trend with different photon energy,. If α in the low energy region has decreased trend of variation with the decreasing of photon energy, this assigned to the existence of band tails. While when α increases trend of variation as the decreases of photon energy, this assigned to the existence of free carrier absorption. When α doesn't change as the photon energy decrease ,the inter band is formed [25].

Urbach tail exists which is as exponential part that exists along the curve of the absorption coefficient and close to the optical band edge, it is dependents on many materials photon energy [26].Urbach rule is shown in the following equation used to determine the width of the formed band tails [27],

$$\alpha = \alpha_0 \; e^{E/E_0} \tag{2.14}$$

Where E_0 is the width of the band tails which is the Urbach energy .

The straight line slope of plotting $\ln(\alpha)$ versus E obtains the energies of entering band.

2.2.6 Dielectric Spectra

Dielectric spectra are the main source for storing the energy of electromagnetic. Refractive index is one of most distinguishing optical features of the dielectric solids, that describes how fast speed of light through the material. It is a complex number having real and imaginary parts depending on the wavelength of the incident optical beam. The connection between the optical wave length and the refractive index is determined by dispersion equation. The dispersive refractive index ($N_{complex}$) can be defined as the following equation [28],

$$N_{complex} = n(\lambda) + iK(\lambda)$$

$$= (\varepsilon_r + i\varepsilon_{im})^{1/2} \quad (2.15)$$

Where, $K(\lambda)$ is the coefficient of extinction,

ε_r and ε_{im} are the real and imaginary dielectric constants, respectively.

The imaginary terms which are shown in equation (2.15) are

The dispersive refractive index which shows in equation (2.15) involve some imaginary terms. This illustrates the dispersion and optical attenuation which the propagating electromagnetic waves through the dielectric solid undergo.

As shown in the following equation, the effective dielectric constant ε_{eff} can be defining in terms of real ε_r and imaginary ε_{im} dielectric constants [29],

$$\varepsilon_{eff} = \varepsilon_r + i\varepsilon_{im} \quad (2.16)$$

The effective dielectric constant ε_{eff} also can be defining in terms of the refractive index $n(\lambda)$ as shown in the following relation [29],

$$\varepsilon_{eff} = n^2(\lambda) \quad (2.17)$$

We obtain the following equation by squaring both sides of equation (2.15),

$$n^2(\lambda) - k^2(\lambda) + 2in(\lambda)k(\lambda) = \varepsilon_r + i\varepsilon_{im} \quad (2.18)$$

By comparing the real and imaginary parts on both sides of relation(2.18), we can obtain the two following equations:

$$K(\lambda)n^2(\lambda) - k^2(\lambda) = \varepsilon_r \qquad (2.19)$$

$$2n(\lambda)K(\lambda) = \varepsilon_{im} \qquad (2.20)$$

By replacing $n^2(\lambda)$ by ε_{eff} in equation (2.19) and $n(\lambda)$ by $(\varepsilon_{eff})^{1/2}$ in equation (2.20), we can obtain ε_r and ε_{im} dielectric as shown in the following relations [29],

$$\varepsilon_r = \varepsilon_{eff} - \left(\frac{\alpha\lambda}{4\pi}\right)^2 \qquad (2.21)$$

$$\varepsilon_{im} = 2\,(\varepsilon_{eff})^{1/2}\,\frac{\alpha\lambda}{4\pi} \qquad (2.22)$$

Where,

$$k = \frac{\alpha\lambda}{4\pi} \qquad (2.23)$$

The normal reflectance in terms of $N_{complex}$is defined by,

$$R = \left|\frac{1 - N_{complex}}{1 + N_{complex}}\right|^2 = \frac{(1-n)^2 + k^2}{(1+n)^2 + k^2} \qquad (2.24)$$

The reflectance R relates to the effective dielectric constant ε_{eff} as in the following equation.

$$R = \frac{(\sqrt{\varepsilon_{eff}} - 1)^2 + k^2}{(\sqrt{\varepsilon_{eff}} + 1)^2 + k^2} \qquad (2.25)$$

Hence, from reflectance (R) data, one can calculate the effective dielectric constant which is necessary to find ε_r and ε_{im}

2.2.7 Drude-Lorentz Model

The effective oscillator models with helps of effective oscillator model use to analyze the imaginary part of dielectric constantε_i. Atoms or molecules of dielectric solid it is possible to consider as a mass of oscillators. Based on Drude-Lorentz model, the dielectric material a blaze the dipole oscillations as the electric field of the electromagnetic waves reacts with it. The electrons fixed with the positively charged molecules that vibrate around an equilibrium position with a given resonant frequency. ε_1 and ε_2 are real and imaginary dielectric constants respectively which is defined as the following equations [30] :

$$\varepsilon_{1(\omega)} = 1 + \chi + \frac{Ne^2}{\varepsilon_0 m_0}(\frac{\omega_0 - \omega^2}{({\omega_0}^2 - \omega^2)^2 + (\gamma\omega)^2} \tag{2.26}$$

$$\varepsilon_{2(\omega)} = \frac{Ne^2}{\varepsilon_0 m_0}(\frac{\gamma\omega}{({\omega_0}^2 - \omega^2)^2 + (\gamma\omega)^2} \tag{2.27}$$

Where, χ : is the susceptibility, N:is the numbers of atoms per unit volume,e:is the electron charge ,γ:is the damping coefficient , ε_0: is the vacuum permittivity ,m_0: is the electron mass,ω_0:material natural frequency and ω:is the incident light frequency .

ε_r is the relative dielectric constant which performs the static dielectric constant ε_{st} at $\omega = 0$

The high frequency permittivity can be specified by the relative dielectric constant at $\omega = \infty$,

$$\varepsilon_r(\infty) = \varepsilon_\infty = 1 + \chi \tag{2.28}$$

While the low frequency material permittivity specified in the existence of static electric fields.

$$\varepsilon_{1(0)} = \varepsilon_{st} = 1 + \chi + \frac{Ne^2}{\varepsilon_0 m_0 \omega_0} \tag{2.29}$$

Chapter Three

Experimental details

3.1 Glass Cleaning

The glass slides of size of 25.4 ×76.2 mm diminsions and 1.2 mm thicknesses were cleaned by using distilled water and alchohol firstely, then they were inserted into a peaker containing H_2O_2 (hydrogen peroxide solution). The peaker was covered by Aluminum foil and inserted in to an ultrusound shaker. The ultrusonic wave vibrations were accompained with a heating process which ended after reaching 70°C. The ultrasound shaker was used to clean organic residues from the substrates. The heating and snaking cycle lasted 40 minutes in an alcohol media. The glass slides became ready to be used in the evaporations process of the films after this cleaning process.

3.2 Thin Films Preparation by Thermal Vacuum Evaporation Technique:

The cleaned glass are used as substrates to produce Ge/ $CdBr_2$ (Germanium /cadmium bromide) thin films in a VCM 600 Physical vapor deposition (PVD) system which is shown in Fig 3.1.

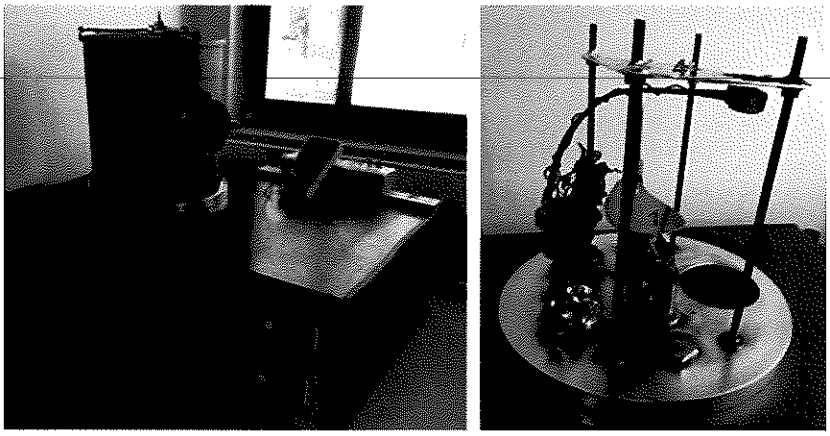

Fig. 3.1. The 600 VCM evaporation system. The system composed of 1. Shutter 2. Evaporation source 3. thickness monitor 4. Substrate.

Prevention rules must be taken in consideration including wearing lab coats and gloves. Highly purity Ge (99.99%) polycrystals, Ge powders were inserted in the tungsten boat, then the chamber evacuated by closing the vent valve, after that the Main powers is turned on, the rough pump turned on and waiting until the pressure reaches (10 mbar), at this point the Turbo Pump is turned on. Pressure continues in decreasing until it reaches (10^{-5} mbar), at this pressure the current control unit was open. After increasing the source current gradually, the shutter was also open .then , thin film of Ge of the thickness of 0.5 μm were obtain at constant evaporation rate of ~ 60 nm/min. After depositing Ge films they were left to cool to room temperature and then used as a substrate for the evaporation of $CdBr_2$ films were prepared from $CdBr_2$ powders (99.99%) inserted in to tungsten heater. $CdBr_2$ films were coated on to glass and Ge substrates to prepare Ge/$CdBr_2$ films. The schematic diagram and optical image of the produced films are shown in Fig 3.2 (a), (b) and (c) and Fig 3.3 (a), (b) and (c) respectively.

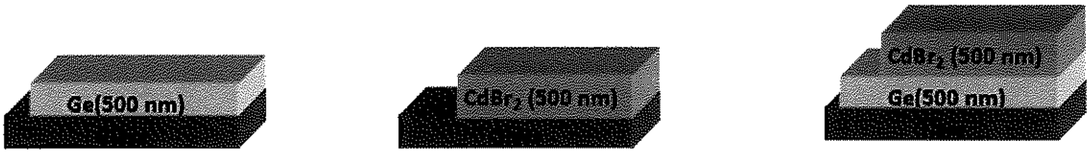

(a) (b) (c)

Fig.3.2. The geometrical diagram of (a) glass/Ge, (b) glass /$CdBr_2$ and (c) glass/Ge/$CdBr_2$ films.

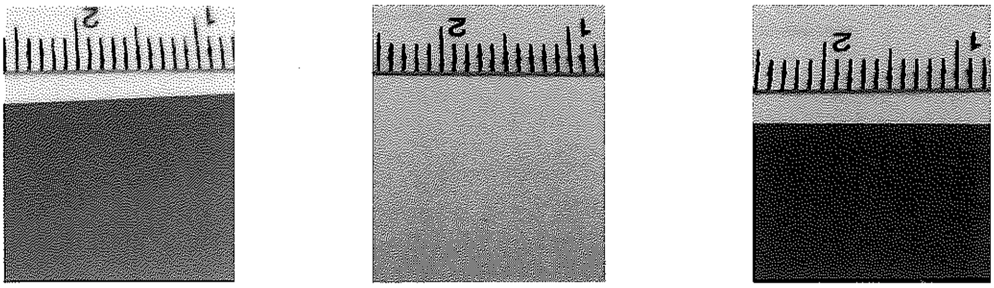

(a) glass/Ge (b) glass /$CdBr_2$ glass/Ge/$CdBr_2$

Fig.3.3.The Optical images for (a) glass/ Ge, (b) glass/$CdBr_2$ and (c) glass/ Ge/$CdBr_2$ thin films.

3.3 Thin Films Analyses:

Ge, $CdBr_2$ and Ge/$CdBr_2$ prepared thin films were subjected to different measuring techniques to explore its structural morphological and optical properties. The X-ray diffraction (XRD) for the studied samples and its optical spectrophotometry are described in the following sections.

3.3.1: The X-ray Diffraction (XRD) Measurements:

Rigaku MiniFlex-600 X-ray diffraction unit (Fig. 3.4), were used to characterize the structure of produced Ge, $CdBr_2$ and Ge/$CdBr_2$ thin films. X-rays were generated from a Kα copper (Cu) anode radiation sources of beam current of 15 mA and average wavelength of 1.5405 Å at a working voltage of 40 KVs. The X–ray is diffracted by the crystal atomic layers. The θ- 2θ scan method used in the diffraction angle ranges of $10^o - 70^o$. Data processing and Instrument control are executed by using a PC. The diffraction patterns were analyzed by the Bragg's diffraction law ($n\lambda = 2d\sin(\theta)$) where λ is the X-ray wave length; d is the distance between the oriented planes and 2θ represents the diffraction angles. The structural analyses are carried out by "Crystdiff" software packages.

Fig. 3.4. X-ray Rigaku diffractometer.

3.3.2 Scanning Electron Microscopy (SEM) Measurements

The surface morphology of the samples tested using a Coxem 200 scanning electron microscope equipped with energy dispersive X-ray spectrometer which shown in Fig. 3.5. The interaction between the electron beam and the studied samples atoms produce signals which provide information about the shape and features of the samples surfaces and the composition of the studied samples.

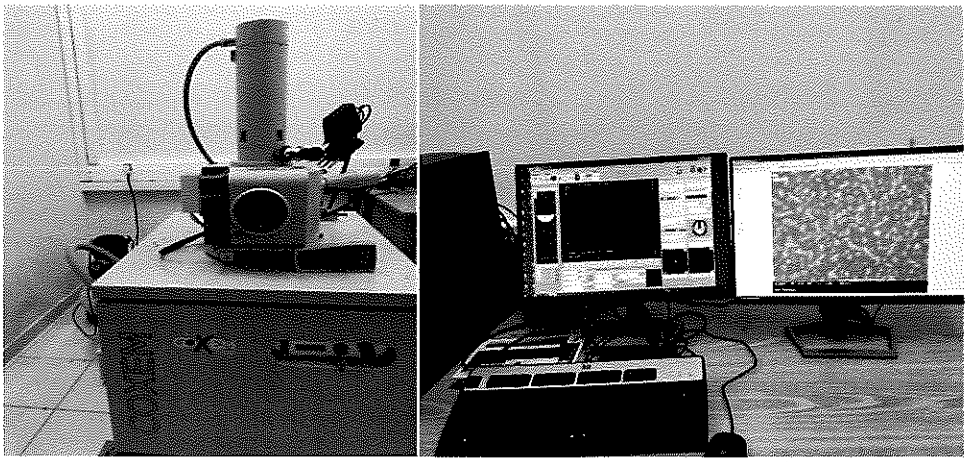

Fig. 3.5. The Scanning Electron Microscopy (SEM)

Fig. 3.6 presents the schematic diagram of the scanning electron microscope (SEM), in which a beam of electrons is directed at a sample and the beam interacts with the materials, which changes the properties of those electrons such as the direction of motion, the angle, the relative phase and its energy.

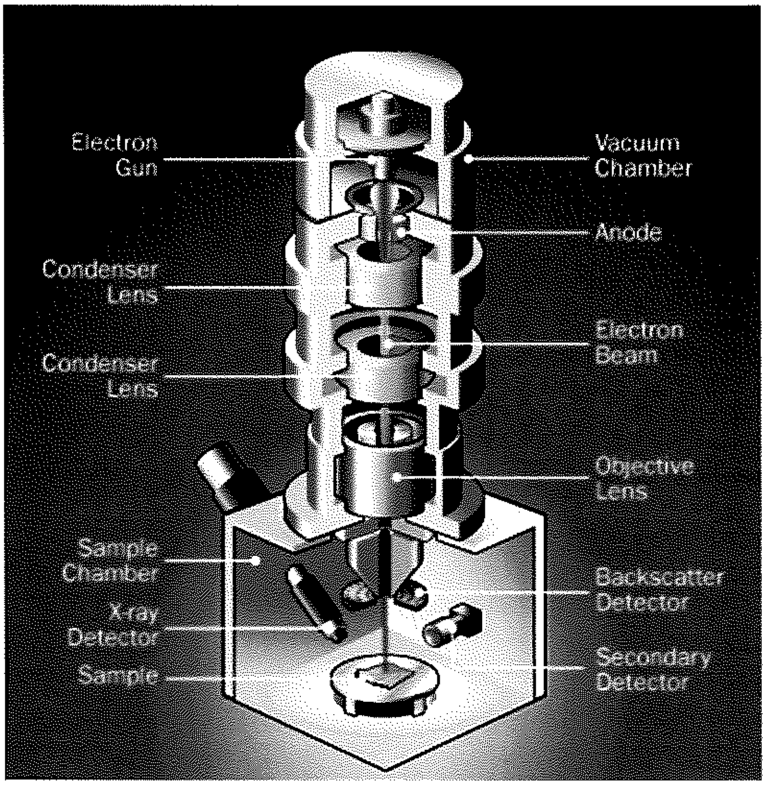

Fig. 3.6. The schematic diagram of SEM. [31]

3.3.3: The Optical Measurements:

Thermo-scientific Evolution 300 ultraviolet–visible light spectrophotometer shown in Fig. 3.7 is used in measuring the optical transmittance and reflectance spectra of the samples. The measurements handled in the spectral wave length range of 190–1100 nm. The system uses a xenon lamp inside the device that emits light of different frequencies across the interested spectrum. The measurements were carried out at scanning speed of 1200 $nm/mins$. The measured data analyzed by using the Vision Pro software packages.

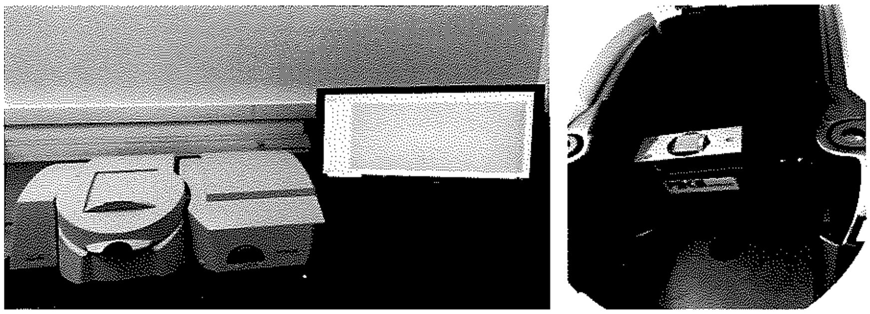

Fig. 3.7. The UV-VIS spectrophotometer.

3.3.4: The Hot Probe Technique:

The hot probe technique is used to identify the type of conductivity (n-type or p-type) of samples. This method consists of heated probe and a standard digital multimeter which shows the type of semiconductors by distinguishing the majority charged carriers. We start the experiment by heating the soldering for a short period. Then a couple of cold probes and hot probes attach to a semiconductor surface under investigation, after that, the hot probes connected to the positive terminal of the multimeter and heater. As well as, the cold probes connected to the negative terminal. While the cold electrode kept constantly connected at the surface of the sample. When the readable value of voltage in the multimeter is positive, the sample indicates that the studying sample is n-type semiconductor sample. Whereas, the negative voltage values indicates represents a p-type semiconductor sample. The Ge and the $CdBr_2$ layer exhibit n-type and p-type of conduction, respectively.

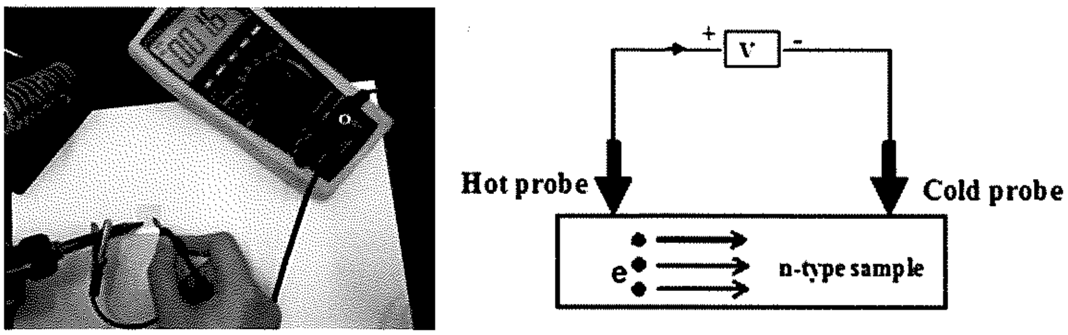

Fig. 3.8. The set-up of hot-probe technique.

Chapter Four

Results and Discussion

4.1 Structural Analysis

The optical images and schematics for the grown films are shown in the inset of Fig.4.1. Fig.4.1 also shows the X-ray diffraction (XRD) patterns of Ge, $CdBr_2$ and Ge/$CdBr_2$.

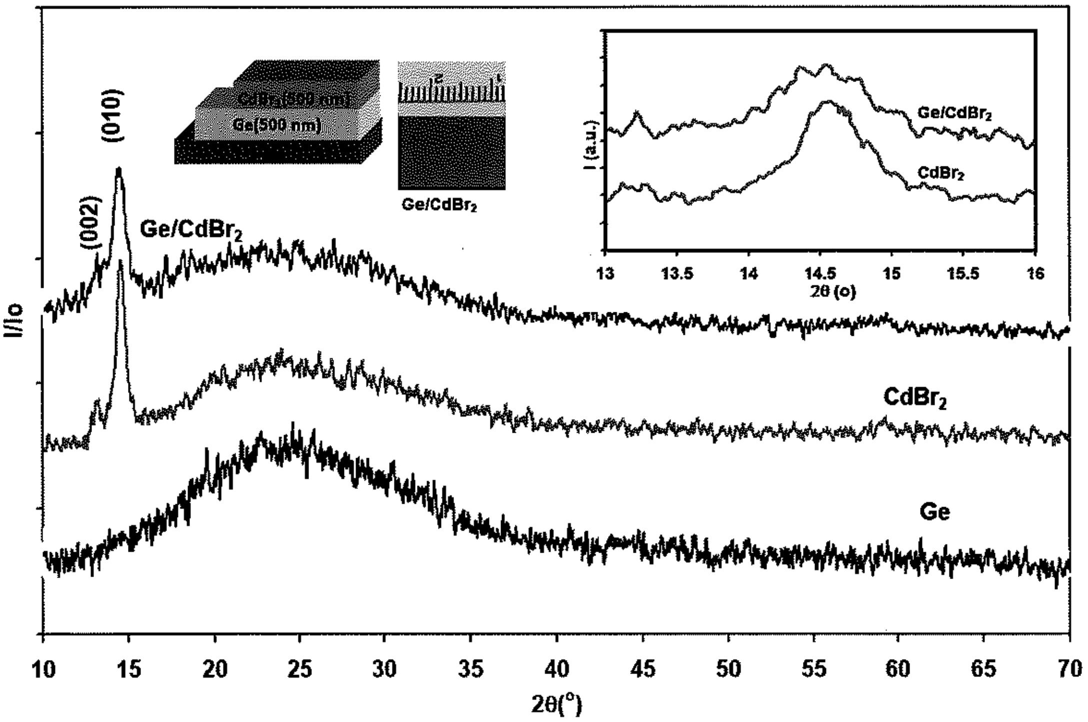

Fig. 4.1. The X-ray diffraction patterns of Ge, $CdBr_2$ and Ge/$CdBr_2$ heterojunction device.

It is clear from the figure that, while $CdBr_2$ films show two diffraction peaks centered at diffraction angles of $2\theta = 13.22$ and 14.58° respectively, the XRD pattern of Ge/$CdBr_2$ also shows two peaks centered at diffraction angles of $2\theta = 13.40^{\circ}$ and 14.50°, respectively. XRD patterns were analyzed by " Crystdiff " software packages. Based on literature data and software analysis, it observed that $CdBr_2$ exhibit hexagonal structure with lattice parameters a = b = 7.20Å and c = 13.86Å. The suitable space group of this structure is shown to be P63mc. [2]. It is also evident from inserted of figure 4.1 that the main diffraction peak of $CdBr_2$ become broader when deposited on amorphous Ge substrates. Repeated calculations of the lattice parameters and other structural parameters are shown in table 4.1. It is clear from the table that the lattice parameters increased along the a - axis and decreased along c-axis. On the other hand, the calculated crystalline sizes decreased while the microstrains defect density and stacking faults increased when deposition is done above Ge layer.

Table 4.1. The parameters of the main peak of $CdBr_2$ and $Ge/CdBr_2$ structures.

		Lattice constant (Å)		D (nm)	$\varepsilon(X10^{-3})$	SF%	$\delta(X10^{12} line/cm^2)$	
Sample	2θ (°)	a-axis	c-axis				a-axis	c-axis
$CdBr_2$	14.58	7.01	13.38	21.51	12.96	0.47	12.90	6.76
$Ge/CdBr_2$	14.50	7.04	13.20	12.38	22.64	0.82	38.93	20.78

Fig.4.1 shows that the maximum peak which was observed for the $CdBr_2$ hexagonal phase at $2\theta = 14.58^{\circ}$ shifts to 14.50°. This shift is accompanied with a decrease in the intensity of the maximum peak from 109.00 to 108.00 Counts/s. Repeating the calculation for $Ge/CdBr_2$ thin films, we observe lattice parameters of a = b = 7.04 Å and c =13.20 Å. From chemical point of view, $CdBr_4$ (which was observed in SEM analysis) and $GeBr_4$ may be formed due to the strong columbic interaction between Ge and Br. The bond lengths of Ge-Br and Cd-Br are 2.32 Å [32] and 2.55 Å [2], respectively. Thus, the columbic force between Ge-Br is stronger than that of Cd-Br. Other probable reason presented by the ionic substitutions of Ge in unoccupied sites of Cd which could be a source for the formation of $GeBr_4$. Namely, as the ionic radii for Ge^{+4}, Cd^{+2} and Br^{-1} are 0.54 [33], 0.97 [2], and 1.93 [2], respectively, Ge replaces vacant sites of Cd. Hence, the increase in the lattice constants values is due to the shorter ionic radius of Ge compared

to Cd [2]. In addition, it observes from table 4.1 that the deposition of the $CdBr_2$ layers onto the Ge substrates change the substrate structural parameters upon substitution of Ge to Cd empty sites .it should be noted that $CdBr_4$ is detected in the SEM analysis while $GeBr_4$ was not indicating that it is formation is less probable. Particularly, as we previously mentioned the crystallite size (D) decrease while, the strain (ε), dislocation density (δ) and stacking fault percentages (SF%) are increased.

Table 4.2. The ionic raduis, electronic configuration, bond length of the samples

Sample	Ionic radius (Å)	Reference	Electronic configuration	Sample	Bond length (Å)	Reference
Cd	0.97	[2]	[Kr] $4d^{10}5s^2$	Br-Br	3.79	[34]
Br	1.93	[2]	[Ar] $4s^2\,3d^{10}\,4p^5$	Cd-Cd	6.54	[33]
Ge	0.54	[33]	[Ar] $3d^{10}\,4s^2\,4p^2$	Cd-Br	2.55	[2]
				Ge-Ge	2.45	[35]
				Ge-Br	2.32	[32]

In reference to table 4.2 it is noted that, the smaller ionic radii of one ion compared to the other in the same structure causes shrinking of the dimensions of unit cell resulting in decrease in the crystalline sizes [36]. Microstrain increases due to the increase in the lattice parameters and due to large lattice mismatches between the amorphous Ge and polycrystalline $CdBr_2$.

4.2 Morphological Analyses

The surface morphology was tested by the scanning electron microscope available in our laboratory. The results are presented in Fig. 4.2. It is evident from Fig. 4.2 (a) that Ge substrates have no distinguishable morphology. No grains appeared in the image indicating the amorphous nature of the films. In contrast, as can be seen from Fig. 4.2 (b)

$CdBr_2$ thin films display irregularly shaped grains shown by white colored points in the figure, in addition to some clusters appearing as dark colored circles. The presence of grains assures the polycrystalline nature of the films. The average grain size of the white colored points is 940 nm. Black colored circular clusters showed a diameter of 4.0 μm. When $CdBr_2$ is coated onto Ge substrates most of the irregularly shaped grains disappeared while the circular clusters remained. They show diameter of 790 nm. It is clear that Ge substrates resulted in a decrease in the cluster sizes. Energy dispersive X-ray analysis on the $CdBr_2$ and Ge/$CdBr_2$ films have shown that the white colored irregularly shaped points are composed of 32.95 at.% Cd and 67.05 at. % Br revealing the chemical formula of $CdBr_2$. On the other hand when the same EDS test is handled for the black colored circles they revealed 20.0 at. % Cd and 80.0 at. % Br. The empirical formula is $CdBr_4$. Hence it is possible to conclude that $CdBr_2$ films contains clusters of $CdBr_4$ as a minor phase.

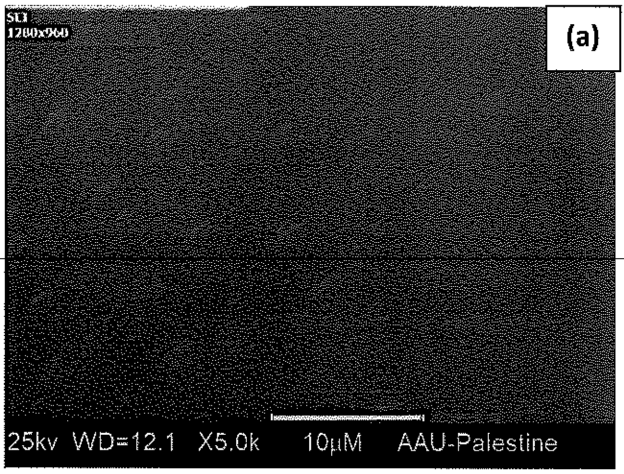

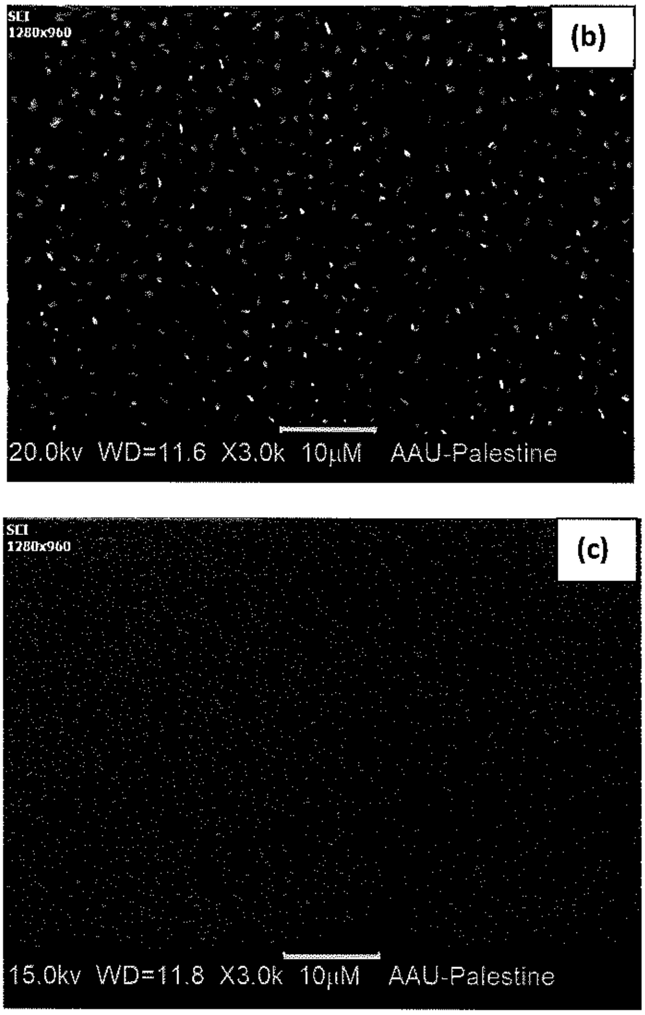

Fig. 4.2. SEM images for (a) Ge film, (b) $CdBr_2$ film and (c) Ge/$CdBr_2$ films

4.3 Optical Analysis

The effects of the Germanium (Ge) substrates on the optical performance of the Cadmium bromide ($CdBr_2$) thin films are investigated by mean of visible light spectrophotometry technique. Transmittance (T) and Reflectance (R) spectra were measured in the wavelength (λ) range of 190–1100 nm of the incident light. The measured transmittance (T) and reflectance (R) spectra for Ge, $CdBr_2$ and Ge/$CdBr_2$ structures are shown in Fig. 4.3 (a) and (b), respectively. As shown from the Fig. 4.3 (a), the transmittance spectrum of $CdBr_2$ film is very high compared to Ge. The spectra of Ge decrease slowly until reaching a sharp absorption edge near to be 3.5 eV with transmission saturation between 1.5-3.5 eV . After that its sharply decrease until reaching 0% at 4.1 eV , as shown in the same figure, there is a transmission saturation which is initiated for E> 1.5 eV . For the $CdBr_2$ films, the transmittance spectra have tendencies of increasing until reaching 3.23 eV. Its exhibits a shoulder and one peak centered at this energy value then its sharply decrease. The T% spectra of $Ge/CdBr_2$ indicates that the effect of deposition of $CdBr_2$ layers on the Ge film become semi transparence when incident light energy (E) is less than 1.8 eV. It is clear from the figure that, a major peak centered at 1.19 eVs existing. Particularly, the reflectance spectra which are presented in Fig. 4.3 (b) show that Ge spectra has a peak at 1.26 eV. The Reflectance of $CdBr_2$ is very low (lower than 5%), the reflectance coefficient doesn't show any significant sharp pattern indicating possible strong absorbance. The peaks of minimum reflectance shift from 1.57 eVs in the reflectance spectra of Ge to 1.32 eVs upon adding the $CdBr_2$ layer is due to higher film thickness. The observed peaks in reflectance and transmittance usually occur because of light interference from different layers, as thickness increase peaks becomes closer.

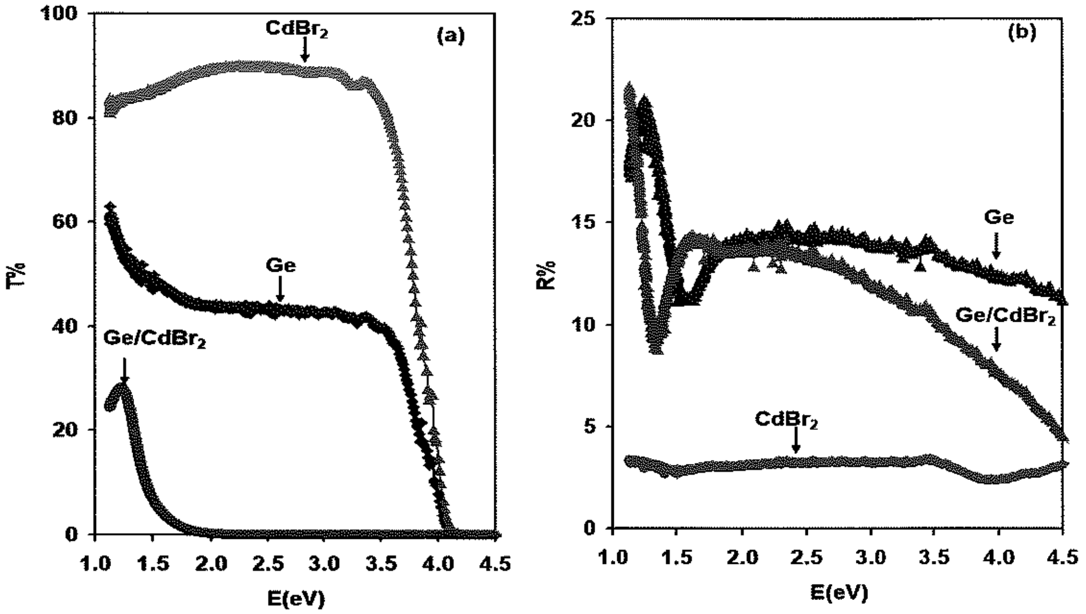

Fig. 4.3. The transmittance (a) and reflectance (b) for $CdBr_2$ and Ge/ $CdBr_2$ heterojunction device.

The absorption coefficient (α) spectra for Ge, $CdBr_2$ and Ge/$CdBr_2$ films are calculated from the measured transmittance (T) and reflectance (R) spectra using equation(2.12)

Where $d = 0.5\ ,0.5\ and\ 1\ \mu m$ for Ge, $CdBr_2$ and Ge/$CdBr_2$ respectively . Both of α and absorbability spectra (R_λ) are calculated and shown in Fig. 4.4. As the figure displayed, α -spectra of $CdBr_2$ start with low absorption coefficient (α) illustrating an increasing trend of variation with decreasing incident photon frequency in the energy range of (1.13 -1.97 eV) This phenomena relate to a free carrier absorption that arises from the existence of free electrons and holes [37], lattice distortion [38] in this region. The region between (1.97 -3.18 eV) is an absorption saturation region. Then, above 3.47 eVs the absorption spectra increase sharply with increasing incident photon energy. On the other hand, Ge spectra show that Ge has low absorption level in the low energy region. α -spectra of Ge show an absorption saturation between (2 - 2.4 eV). α values sharply increase with increasing E meaning that the strong absorption have already started. on the other hand, Ge/$CdBr_2$ spectra show that there is possible formation of a band tail in the low energy level then, the spectra sharply increase which indicate to strong absorption exist. After that, the spectra behavior indicates to saturation. [39]

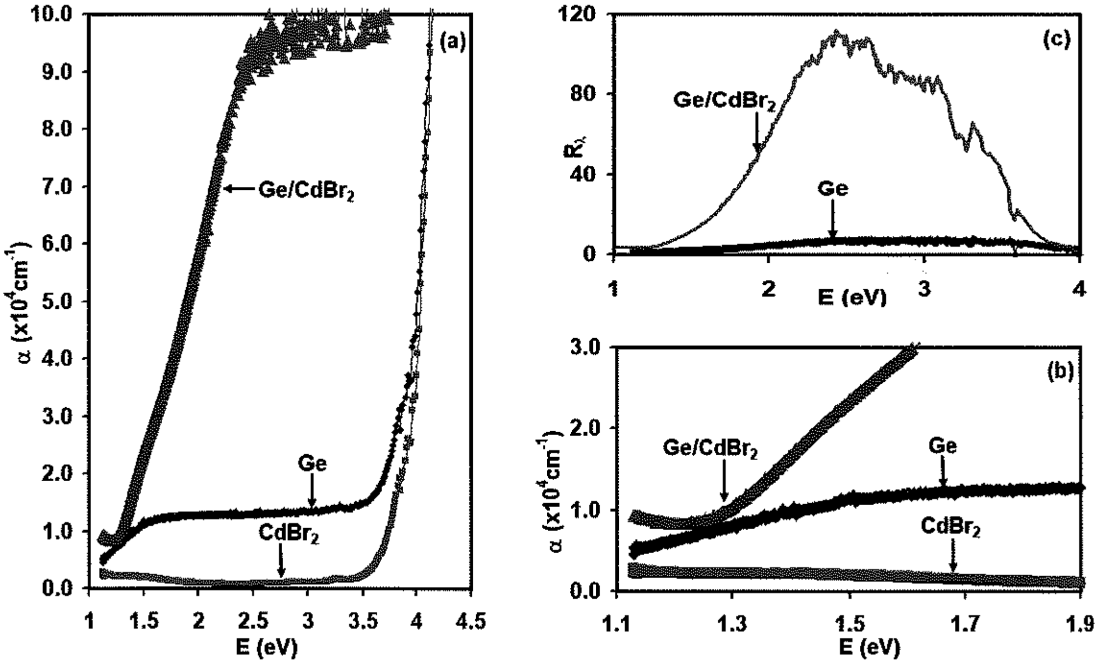

Fig. 4.4. The optical absorption coefficient spectra (a)in all region (b) in low region only for Ge, $CdBr_2$ and Ge/$CdBr_2$ heterojunction device and (c) the absorbability for Ge, and Ge/$CdBr_2$ heterojunction device.

The absorbability light spectra for Ge/$CdBr_2$ ($R_\lambda = \frac{\alpha_{Ge/CdBr2}}{\alpha_{CdBr2}}$) and the absorbability light spectra for Ge ($R_\lambda = \frac{\alpha_{Ge/CdBr2}}{\alpha_{Ge}}$) are shown in Fig. 4.4 (c). It illustrates that; in visible region of light, the absorption coefficient of $CdBr_2$ increases nearly 115 times when it deposit on Ge. The remarkable enhancement is a promising feature as it indicates possible application invisible light communications. Fig. 4.5 shows ln(α)-E variations for Ge, $CdBr_2$ and Ge/$CdBr_2$ heterojunction device that used to determine if there is a band tail or not in the low absorption region by the help of Urbach rules [27] Urbach rules assumes exponential band tail distribution which defined by equation (2.14). This equation is used to get the band tails width. There is no tail if the reciprocal value of the slope (E_0) of the linear variation of $\ln(\alpha)$ versus $E > \frac{E_g}{2}$ but if it $< \frac{E_g}{2}$ there will be a band tail. As a result of calculation, the expected energy bands tail widths for Ge, and Ge/CdBr$_2$ are 0.48 eV, and 1.13 eV, respectively. Hence CdBr$_2$ doesn't have band tail because $E_0 = 2.13 > \frac{E_g}{2} = \frac{0.93}{2}$ while Ge/CdBr$_2$ has a band tail. The formation of this band tail is assigned to the orbital overlapping between Ge and CdBr$_2$. Urbach equation is not valid for CdBr$_2$ film due to the increasing of absorption coefficient with decreasing energy. Such behavior indicates the existence of free carrier absorption.

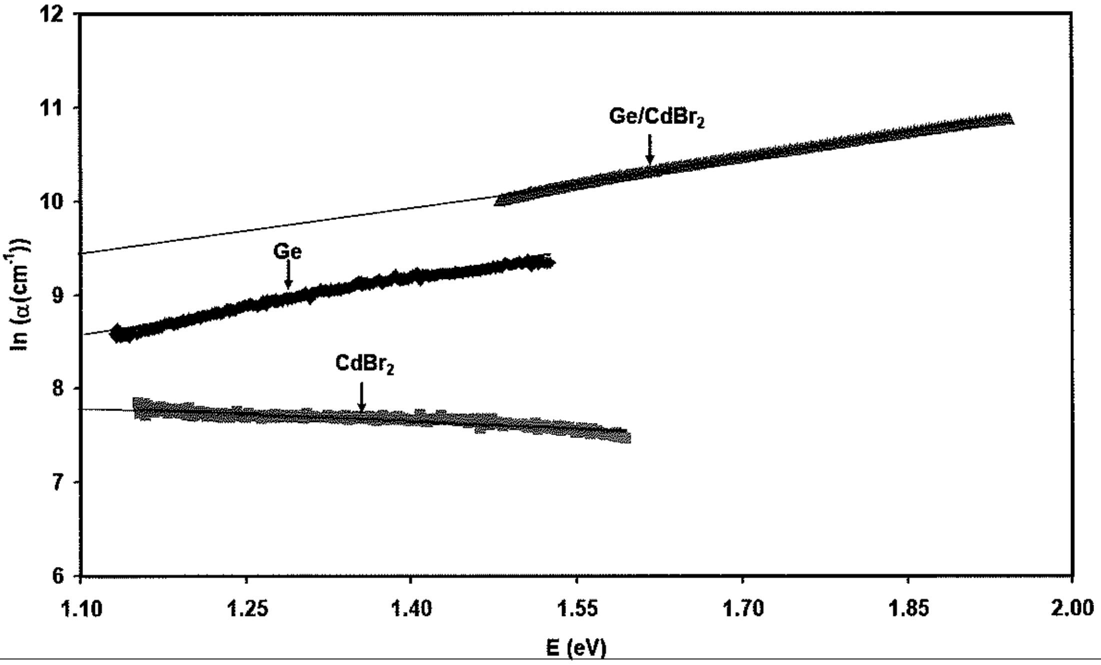

Fig. 4.5. The ln(α)-E variations for Ge, CdBr$_2$ and Ge/CdBr$_2$ heterojunction device.

The absorption coefficient spectra provide information about the energy band gaps (E_g) of Ge, CdBr$_2$ and Ge/CdBr$_2$, respectively. Fig. 4.6 (a), (b), (c) and (d) represent the plotting of Tauc's equation for Ge, CdBr$_2$ and Ge/CdBr$_2$, respectively. The effect of adding CdBr$_2$ on the optical energy band gap of Ge film is determined with the help of the Tauc's equation ((2.13) [23]). Where the indirect allowed energy band gap for Ge, $CdBr_2$ and Ge/$CdBr_2$ interface were determined from the plotting of the $(\alpha E)^{1/2} - E$ variations which are presented in Fig. 4.6(a), (c) and (d) respectively. The straight lines which cross the energy (E)-axis revealed energy band gap values of 3.04, 3.45 eV and 3.23eV for Ge, $CdBr_2$ and Ge/$CdBr_2$ films, respectively. The reported band gap value of Ge being 3.01 is ascribed to Γ_{8v} to Γ_{6c} transition in the first Brillouin zone of Ge [40] and the band gap value of $CdBr_2$ is reported to be 3.32 eV [2]. In addition, the direct forbidden energy band gap were determined from the plotting of $(\alpha E)^{2/3} - E$ which illustrated in Fig. 4.6 (b) that reveal another energy band gap value of 1.0 eV for Ge. The value of the energy bands gap being 1.0 eV is very close to the reported value being 0.9 eV. This band gap value may be ascribed to Γ_{8v} to Γ_{7c} transition in the first Brillouin zone [40]. Practically, when dealing with heterojunctions at room temperature, it usual to choose the lowest value of the energy band gap. Recalling that the electron affinity of n-type Ge is 4.0 eVs [41] and that of p-type $CdBr_2$ is 3.27 eV [42], then the conduction bands offset ($\Delta Ec = |q\chi_{CdBr2} - q\chi_{Ge}|$) are 0.63 eV. The difference between the energy bands gaps (ΔEg=2.11 eV). The valence-band offset ($\Delta Ev = |\Delta Eg - \Delta Ec|$) turns out to be 1.48 eVs. On the other hand, it's mentioned that the work functions values of Ge and $CdBr_2$ are 4.37 and 6.38 eV respectively [43], [5] so that the built in voltage $(q\varphi_{CdBr2} - q\varphi_{Ge})$ turns out to be 2.01 eVs. The values are high enough to nominate Ge/$CdBr_2$ interfaces for optoelectronic applications.

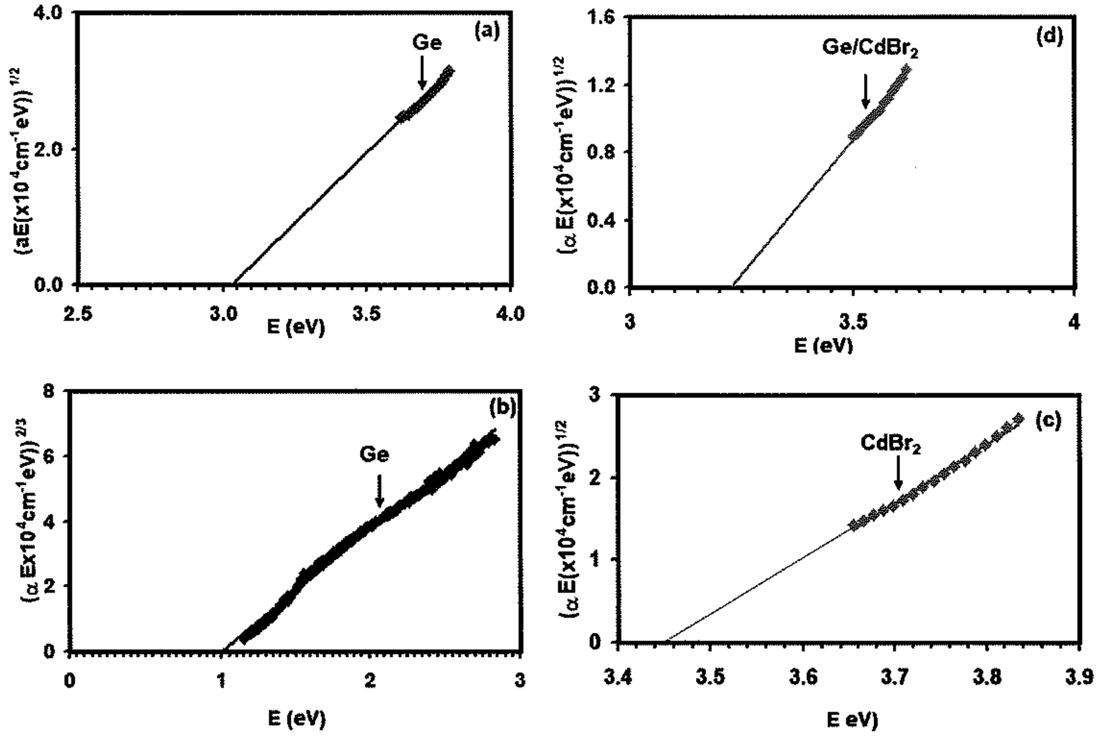

Fig. 4.6.The $(\alpha E)^{1/2}$-E (a) for Ge (c) for $CdBr_2$ and (d) for Ge/$CdBr_2$ heterojunction.

(b) The $(\alpha E)^{3/2}$-E for Ge .

4.4 Dielectric Properties

The Dielectric constant is known as the fundamental intrinsic property of the material while the real part of the dielectric function displays that how much the speed of light will be within the material [44].To investigate possible applications of the Ge/$CdBr_2$ heterojunction, the respective real (ε_r) and imaging part of the relative dielectric spectra are estimated for the studied samples. ε_r spectra which is calculated by using equation (2.21) is illustrated in Fig. 4.7. As shown in the figure $CdBr_2$ spectra exhibit a broaden peak at 3.42 eVs. It mentioned that $CdBr_2$ emission in UV bands is initiated at 3.3-3.4 eVs [44]. Ge spectra show that the dielectric constant increases as the photon energy decrease; it has a peak at infrared region which is centered at 1.25 eVs. Also it has another peak in ultraviolet region centered at 3.47 eVs. It mentioned that Semiconductor films with 1.25 eV energy band gaps have a high transmission in the IR thermal emission region and high absorption coefficient in the solar spectral region [45]. On the other hand, the peak centered at 3.47 eVs is related the intense peaks of the excitonic excitations [45]. It mentioned that the reflection intensity monotonously decreases in the ultraviolet spectral region from Ge surface. This occurs due to amorphization if the doses are low and because of forming nanoporous structure of interwoven nanowires for the higher doses in the near-surface implanted Ge layer [46]. As shown in the figure, Ge/$CdBr_2$ heterojunction spectra have a minimum peak centered at 1.32 eVs, while its spectra made a red shift and increase and the maximum point couldn't be reached.

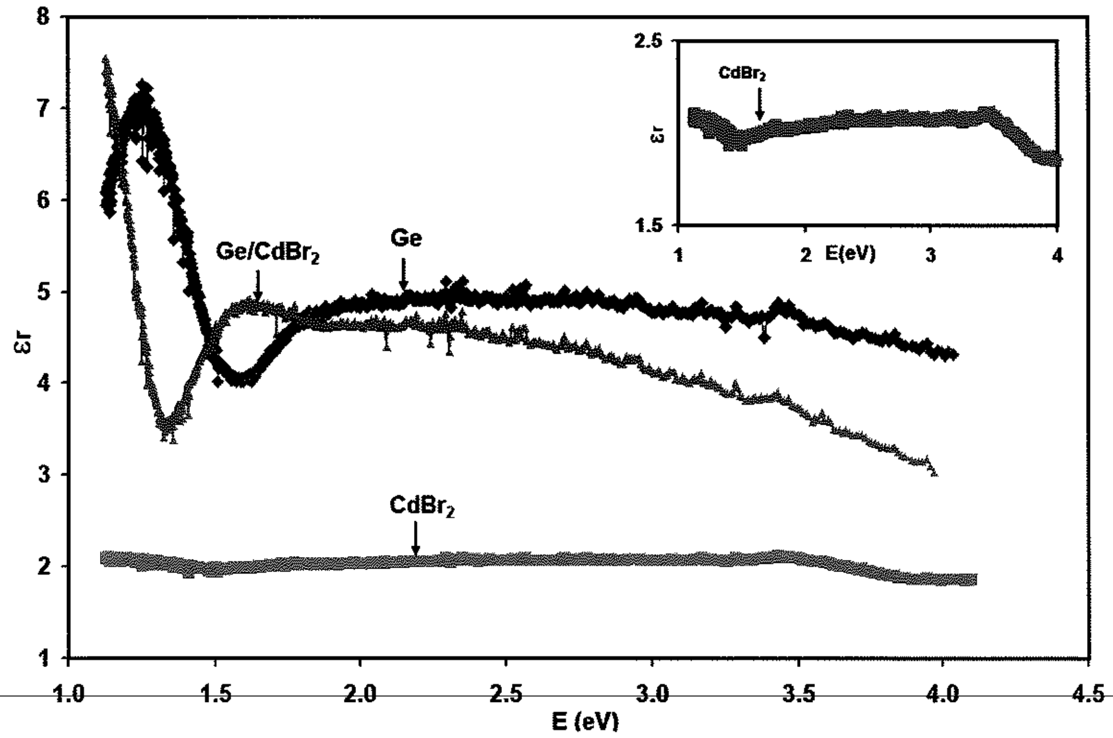

Fig. 4.7. The real part of the dielectric spectra for Ge, $CdBr_2$ and Ge/$CdBr_2$ heterojunction.

To gain information about the optical conductivity ($\sigma(w) = (\varepsilon_{im} w/4\pi)$; where, w is the angular frequency), free electron mobility and electron Plasmon interaction of the samples under realization, the imaginary part (ε_{im}) of the dielectric constant spectra is calculated and analyzed. The ε_{im} for the Ge, $CdBr_2$ and Ge/$CdBr_2$ heterojunctions are presented in Fig. 4.8. In accordance with this figure, Ge spectra increase slowly until the incident energy values reaches 1.37 eVs, then it is slowly decrease until the incident energy values reaches 3.55 eV, after that it is sharply increasing. $CdBr_2$ spectra behavior is partially similar to Ge spectra, ε_{im} of $CdBr_2$ slowly decreased until the incident energy value reaches 1.81 eV, and then nearly remain constant until the incident energy reaches 3.58 eVs. After that it starts to increase following a sharp trend of variation. Ge/$cdBr_2$ spectra display a decreasing trend of variation with the increase of the incident light energy until it reaches 1.26 eVs. Then, it begins to increase sharply until the incident energy values reaches 2.42 eV, after that it starts to decrease following a sharp trend of variation. The sharp increase of ε_{im} donates to increase of the conductive behavior of material, which is concerned to the interband transition of electrons from the valence band to the conduction band, where it become available to conduct current.

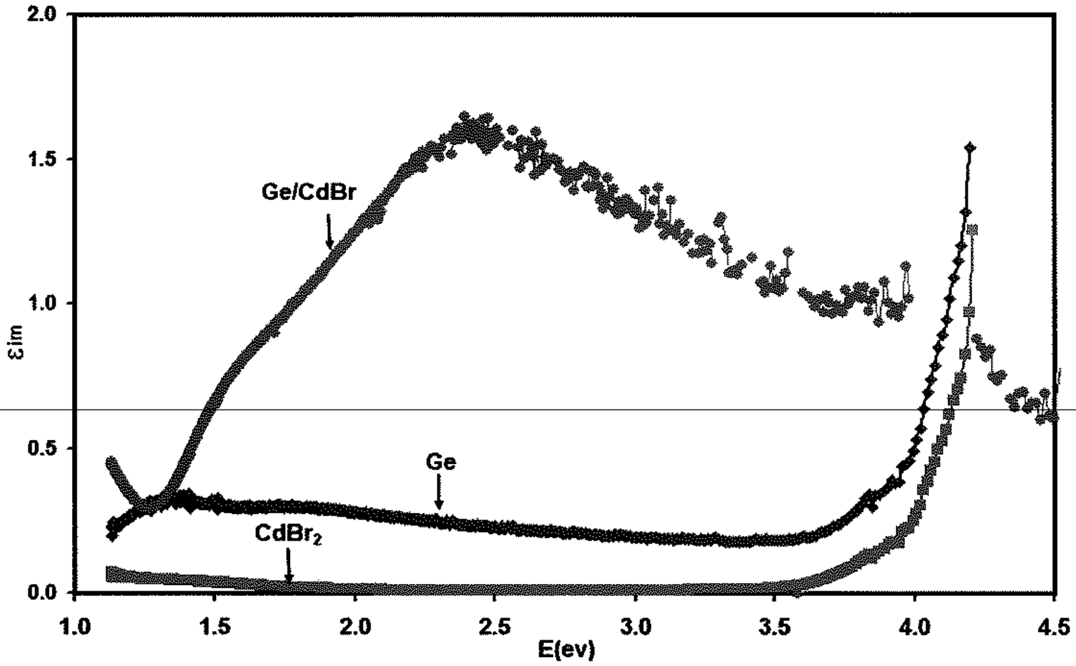

Fig. 4.8. The imaginary part of the dielectric spectra for Ge, $CdBr_2$ and Ge/$CdBr_2$ heterojunction.

In order to understand and get information about the Plasmon-electron interaction in the Ge, $CdBr_2$ and Ge/$CdBr_2$ heterojunctions, in accordance with Drude-Lorantz approach, the imaginary part of the dielectric constant spectra is modeled through the relation [47],

$$\varepsilon_{im} = \sum_{i=1}^{k} \frac{w^2{}_{pei} w}{((w^2{}_{ei} - w^2)^2 + w^2 \tau_i{}^{-2})} \tag{4.1}$$

Where, k is the number of dominant linear oscillators, $w = 2\pi f$ is the angular frequency of the incident light, $w_{pe} = \sqrt{4\pi n e^2/m^*}$ represents the electron bounded Plasmon frequency, w_e indicate to the reduced resonant frequency, τ is the average of scattering time which is the inverse of the damping coefficient, increase in τ means the electronic friction will decrease. This behavior raise from the decreasing in the number of impurities (defect) ions which available for scattering. m^* represents the effective mass of free carrier and n represent the free electron density. Mobility of the free-carrier is also calculated by the formula $\mu = e\tau/m^*$. The experimental data was reproduced by fitting Equation (4.1) through substituting the values of the effective mass as $m^*_{\mathrm{e-Ge}} = 0.55\, m_o$[48]and $m^*_{\mathrm{h-CdBr2}} = 0.44\, m_o$[5] and The reduce effective mass for carriers in Ge/$CdBr_2$ layer was calculated using $\frac{1}{m^*} = \left(\frac{1}{m_1} + \frac{1}{m_2}\right)^{-1}$ [2], by using the effective mass value for Ge and $CdBr_2$, the effective mass of Ge/$CdBr_2$ calculated to be 0.204 m_o. Fig. 4.9 illustrate the fitting plots of $\varepsilon_{\mathrm{im}}$ spectra of (a) Ge, (b) $CdBr_2$and (c) Ge/$CdBr_2$ layers where the black colored curve represents the theoretical fitting data of the ε_{im} spectra. Fig.4.9 indicates that the values of experimental data of imaginary dielectric constant are almost the same with the fitted ones.

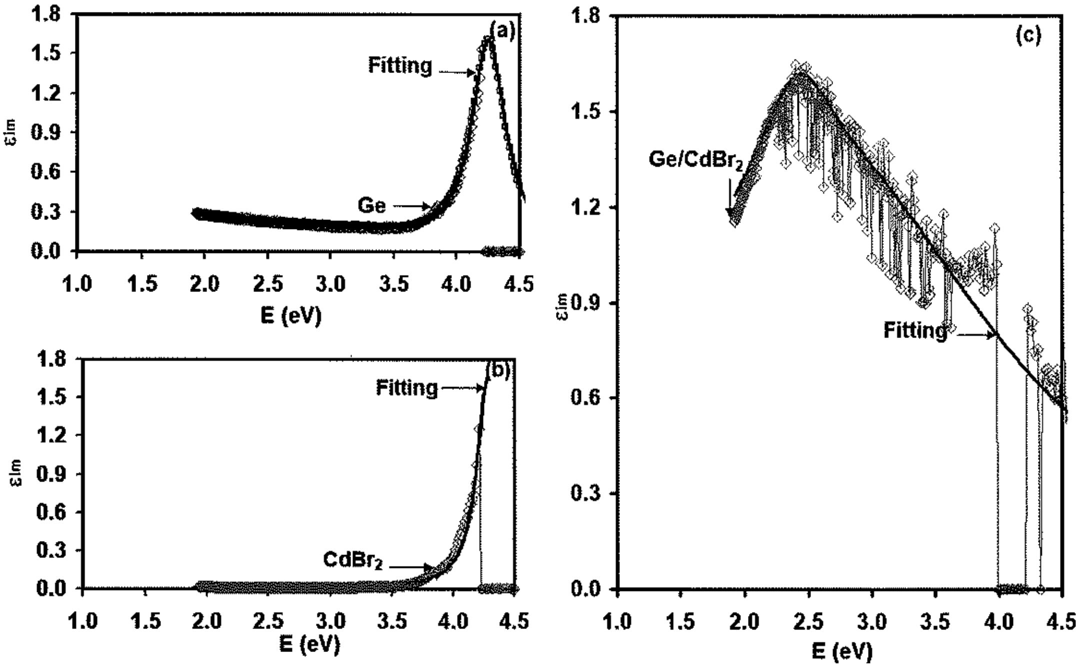

Fig. 4.9. The imaginary part of the dielectric spectra for (a) Ge, (b) $CdBr_2$ and (c) Ge/$CdBr_2$ heterojunction. The black colored plots represent the fitting which is achieved by Eqn. (4.1).

The fitting parameters which show the best correlation between the experimentally and theoretical values are tabulated in Table 4.3 (a), (b) and (c) respectively, for Ge, $CdBr_2$ and Ge/ $CdBr_2$. Generally, the scattering time decreases as the oscillator frequency (w_e) increases which indicate to the increasing of the damping coefficient leading to more electronic frictional forces. Electronic frictional forces increase from the interfacial electronic interactions [49, 50] that cause distortions of the wave functions of conduction electron [51]. In accordance with the table 4.3 (c), the scattering time (τ) for the first oscillators (τ_1) was 5 fs, when we reached the last oscillators (τ_5) it becomes 0.2 fs. The increasing in the oscillator frequency cause increasing in the electronic friction where the photon energy increases enough to activate more defects [49]. The presence of defects and impurities increasing the electronic friction. Also, increasing the oscillator energy (E_e) indicates to the increasing in the kinetic energy of electrons that in turn enhances the scattering mechanism which freeing electrons. [42].As it is readable from the Table 4.3 (c), the resonance frequency (w_e) when the $CdBr_2$ layers exists at the surface of the Ge substrate increased from $w_{e1} = 1.90 \times 10^{15}$ Rad/s to $w_{e5} = 5.00 \times 10^{15}$ Rad/s when we transit from the first oscillator number ($i = 1$) toward the last one ($i = 5$). In addition, the free electron density (n_l) values Ge, $CdBr_2$ and Ge/ $CdBr_2$ are found to be 4.00×10^{18} cm^{-3}, 0.20×10^{18} cm^{-3} and 6.00×10^{18} cm^{-3} ,respectively. It is important to notice that the free electron density is increased due to depositing on $CdBr_2$ by Ge. It is clear from the table that, resonant frequency (w_{e1}) increased as the oscillator (k) increased. Moreover, the drift mobility (μ) is decreased when we move from the first oscillator (τ_1) to the second oscillator (τ_2) then it is remaining constant. It is also observed from the tables that, the electron scattering time for the first oscillator ($k = 1$) for amorphous Ge (τ_1=1.50 fs) is larger than that of $CdBr_2$ (τ_l=1.00 fs) indicating that the value of the electronic friction coefficient in Ge is higher than it is for the $CdBr_2$ films. Using Ge as a substrate of the $CdBr_2$ layers increases the scattering time of the Ge/ $CdBr_2$ junction to a value of 5.00 fs. For the first oscillator ($k = 1$), the drift mobility (μ) for the Ge, $CdBr_2$ and Ge/ $CdBr_2$ interface are found to be 4.80 cm^2/Vs, 4.00 cm^2/Vs and 35.96 cm^2/Vs, respectively. This indicates to the enhancement of the drift mobility due to the exchange of glass substrate of $CdBr_2$ by Ge. The improvement of μ makes the device more suitable for transistor technology and wave filter [52]. It is good to indicate that the first oscillator ($k = 1$) is the most accurate from other oscillators because this series came from Taylor expansion, so that we use it in the comparable.

Table 4.3 (a): The optical conductivity parameters for Ge thin film.

i	1	2	3	4	5
τ(fs)	1.5	1.0	0.5	0.6	2.0
n (x10^{18} cm^{-3})	4.0	6.0	15.0	9.0	70.0
ω_e (x10^{15} Rad/s)	2.5	3.0	4.0	5.0	6.5
E(eV)	1.6	2.0	2.6	3.3	4.2
ω_p (GHz)	1.6	2.0	3.1	2.4	6.7
μ (cm^2/Vs)	4.80	3.20	1.60	1.92	6.39

Table 4.3 (b): The optical conductivity parameters for $CdBr_2$ thin film.

i	1	2	3	4	5
τ(fs)	1.0	0.7	0.1	6.0	3.0
n (x10^{18} cm^{-3})	0.2	2.0	0.1	0.1	40.0
ω_e (x10^{15} Rad/s)	1.0	2.0	3.0	7.0	6.5
E(eV)	0.7	1.3	2.0	4.6	4.3
ω_p (GHz)	0.4	1.3	0.3	0.3	5.7
μ (cm^2/Vs)	4.00	2.80	0.40	23.98	11.99

Table 4.3 (c): The optical conductivity parameters for Ge/ $CdBr_2$ thin film.

i	1	2	3	4	5
τ(fs)	5.0	1.0	0.2	0.2	0.2
n (x10^{18} cm^{-3})	6.0	7.0	40.0	40.0	100.0
ω_e (x10^{15} Rad/s)	1.9	3.7	4.0	4.5	5.0
E(eV)	1.2	2.4	2.6	3.0	3.3
ω_p (GHz)	2.9	3.2	7.6	7.6	12.0
μ (cm^2/Vs)	35.96	7.19	1.44	1.44	1.44

Chapter Five

Conclusion

In this master thesis we have focused on the formation of new class of heterojunction devices made of amorphous Ge as substrates for coating $CdBr_2$ these films. The growth nature of the double layer was investigated by structural techniques revealing amorphous /polycrystalline interfaces with large lattice misfits. The Ge/$CdBr_2$ bilayers are found appropriate for optical and optoelectronic applications of $CdBr_2$ and Ge enhanced the light absorbability of $CdBr_2$ abruptly. The optical conductivity parameters also improved. one may read a plasmon frequency value of 12 GHz for these films. The formats drift mobility also improved reaching values that nominate the Ge/$CdBr_2$ devices for use in thin film transistor and communication technologies.

References

[1] Plucinski, K. J., and G. Lakshminarayana. “Operation by acentricity in the CdBr2 nanolayers.” *Physica E: Low-dimensional Systems and Nanostructures* 56 (2014): 348-350.

[2] Qasrawi, A. F., and Areen A. Hamarsheh. “Band offsets, electron affinities and optical dynamics at the CdBr2/SiO2 interfaces.” *Optik* 243(2021): 167467.

[3] Wang, Fei, Lemin Jia, Ying Ding, Haihuai Cai, Wei Zheng, and Feng Huang. “Ultra-Long Van Der Waals CdBr2 Micro/Nanobelts.” *Small Methods* 4 (2020): 2000501.

[4] Lakshminarayana, G., A. M. El-Naggar, G. L. Myronchuk, E. Gondek, A. H. Reshak, P. Czaja, and I. V. Kityk. “Laser-stimulated Pockels effect in CdBr2/Cu polymer nanocomposites.” *Physica E: Low-dimensional Systems and Nanostructures* 118 (2020): 113904.

[5] Qasrawi, Atef Fayez, and Areen A. Hamarsheh. "Au/CdBr2/SiO2/Au Straddling-Type Heterojunctions Designed as Microwave Multiband Pass Filters, Negative Capacitance Transistors, and Current Rectifiers." *physica status solidi (a)* 218, no. 22 (2021): 2100327.

[6] Wu, Di, Jiawen Guo, Chaoqiang Wang, Xiaoyan Ren, Yongsheng Chen, Pei Lin, Longhui Zeng et al. “Ultrabroadband and High-Detectivity Photodetector Based on WS2/Ge Heterojunction through Defect Engineering and Interface Passivation.” *ACS nano* 15(2021):10119-10129

[7] Böckle, Raphael, Masiar Sistani, Boris Lipovec, Darius Pohl, Bernd Rellinghaus, Alois Lugstein, and Walter M. Weber. “A Top-Down Platform Enabling Ge Based Reconfigurable Transistors.” *Advanced Materials Technologies* 7(2021): 2100647.

[8] Tripathy, Manas Ranjan, Ashish Kumar Singh, A. Samad, Prince Kumar Singh, Kamalaksha Baral, and Satyabrata Jit. “Impact of heterogeneous gate dielectric on DC, RF and circuit-level performance of source-pocket engineered Ge/Si heterojunction vertical TFET.” *Semiconductor Science and Technology* 35, no. 10 (2020): 105014.

[9] Kadri, Emna, Khaled Dhahri, Régis Barillé, and Mohamed Rasheed. "Novel method for the determination of the optical conductivity and dielectric constant of SiGe thin films using Kato-Adachi dispersion model." *Phase Transitions* 94, no. 2 (2021): 65-76.

[10] Tsybeskov, Leonid, Theodore I. Kamins, Xiaohua Wu, and David J. Lockwood. "Axial Silicon-Germanium Nanowires: Properties and Device Applications." *ECS Transactions* 98, no. 2 (2020): 13.

[11] El-Naggar, A. M., A. A. Albassam, K. Ożga, M. Szota, and I. V. Kityk. "UV-Induced Anisotropy In CdBr2-CdBr2: Cu Nanostructures." Archives of Metallurgy and Materials 60,no.3 (2015):2029-2023

[12] Shin, Sang-Ho, Yikai Liao, Bongkwon Son, Zhi-Jun Zhao, Jun-Ho Jeong, Chuan Seng Tan, and Munho Kim. "A highly ordered and damage-free Ge inverted pyramid array structure for broadband antireflection in the mid-infrared." *Journal of Materials Chemistry C* 9, no. 31 (2021): 9884-9891.

[13] Fadaly, Elham MT, Alain Dijkstra, Jens Renè Suckert, Dorian Ziss, Marvin AJ van Tilburg, Chenyang Mao, Yizhen Ren et al. "Direct-bandgap emission from hexagonal Ge and SiGe alloys." *Nature* 580, no. 7802 (2020): 205-209.

[14] Mora-Herrera, D., Mou Pal, and F. Paraguay-Delgado. "Facile solvothermal synthesis of Cu2ZnSn1-xGexS4 nanocrystals: Effect of Ge content on optical and electrical properties." *Materials Chemistry and Physics* 257 (2021): 123764.

[15] Layasree, S., and A. Deepak. "Simulation and Comparison of Current Voltage Characteristics of Si and Ge based Bio Field Effect Transistor by Varying Oxide Thickness to Get Better Sensitivity." *Revista Geintec-Gestao Inovacao E Tecnologias* 11, no. 2 (2021): 1066-1083.

[16] Warren, B. E. "X-ray diffraction methods." *Journal of applied physics* 12, no. 5 (1941): 375-384.

[17] Nguyen, Thanh-Dinh, Egoitz Sierra, Harkaitz Eguiraun, and Erlantz Lizundia. "Iridescent cellulose nanocrystal films: the link between structural colour and Bragg's law." *European Journal of Physics* 39, no. 4 (2018): 045803.

[18] Qasrawi, A. F., and Olfat A. Omareya. "In situ observations of the permanent structural modifications, phase transformations and band gap narrowing upon heating of Cu2Se/Yb/Cu2Se films." *Journal of Alloys and Compounds* 785 (2019): 1160-1165.

[19] Rath, Siddharth Sankar. Comparison of CPFEM and spectral solution methods in prediction of strains near grain boundaries in a uniaxially loaded oligocrystalline tensile specimen. Michigan State University, 2016: 10128182.

[20] Svetikov, V., I. Ivonin, A. Koshelev, L. Velikov, Yu Vorobiev, A. Goltsov, and V. Yankov. "Suppression of lateral modes in wide aperture laser diodes by digital planar holograms." In *High-Power Diode Laser Technology and Applications IX*, SPIE, vol. 7918, 2011 pp. 192-200.

[21] Qasrawi, A. F., and Hadil D. Aloushi. "In situ observation of heat-assisted hexagonal-orthorhombic phase transitions in Se/Ag/Se sandwiched structures and their effects on optical properties." *Journal of Electronic Materials* 48, no. 12 (2019): 7906-7914.

[22] Fox, Mark. "Optical properties of solids." (2002): 1269-1270.

[23] Makuła, Patrycja, Michał Pacia, and Wojciech Macyk. "How to correctly determine the band gap energy of modified semiconductor photocatalysts based on UV–Vis spectra." *The journal of physical chemistry letters* 9, no. 23 (2018): 6814-6817.

[24] Sun, Greg. "Intersubband approach to silicon based lasers—circumventing the indirect bandgap limitation." *Advances in Optics and Photonics* 3, no. 1 (2011): 53-87.

[25] Pankove, Jacques I. *Optical processes in semiconductors.* Courier Corporation, 1975.

[26] Wager, John F. "Real-and reciprocal-space attributes of band tail states." *AIP Advances* 7, no. 12 (2017): 125321.

[27] Seyam, M. A. M., & Ibrahim, E. M. Annealing effects on the structural and optical parameters of Cu3In17Se80 thin films.Journal of Solids .(2010)

[28] Hammou, Brahim Ait, Abdelhamid El Kaaouachi, Abdellatif El Oujdi, Adil Echchelh, Said Dlimi, Chi-Te Liang, and Jamal Hemine. "Modeling the Bulk and Nanometric Dielectric Functions of Au and Ag." *Magnetic Skyrmions* (2021): 67.

[29] Qasrawi, Atef, Seham Alharbi, and Najla KJhusayfan. “Thickness and annealing effects on the structural and optical conductivity parameters of zinc phthalocynine thin films”. *Digest journal of Nanomaterials and Biostructures* 15, no.2 (2020):471-482.

[30] Wooten, Frederick. "Optical properties of solids." *American Journal of Physics* 41, no. 7 (1973): 939-940.

[31] Souza, G. G. B., and J. D. Wieser. "A reinvestigation of the structure of GeBr4 by electron diffraction." *Journal of Molecular Structure* 25, no. 2 (1975): 442-444.

[32] Boeyens, J. C. A. "Electrostatic calculation of bond energy." *South African Journal of Chemistry* 26, no. 3 (1973): 94-105.

[33] Chung, Hoon-Taek, Jin-Gyun Kim, and Ho-Gi Kim. "Dependence of the lithium ionic conductivity on the B-site ion substitution in (Li0. 5La0. 5) Ti1− xMxO3 (M= Sn, Zr, Mn, Ge)." *Solid State Ionics* 107, no. 1-2 (1998): 153-160.

[34] Han, Aiying, Hao Su, Guohong Xu, Maroof Ahmad Khan, and Hui Li. "Synthesis, crystal structures, and luminescent properties of Zn (ii), Cd (ii), Eu (iii) complexes and

detection of Fe (iii) ions based on a diacylhydrazone Schiff base." *RSC Advances* 10, no. 39 (2020): 23372-23378.

[35] Aldrich, D. B., R. J. Nemanich, and D. E. Sayers. "Bond-length relaxation in Si 1− x Ge x alloys." *Physical Review B* 50, no. 20 (1994): 15026.

[36] Shashidharagowda, H., and Shridhar N. Mathad. "Effect of incorporation of copper on structural properties of spinel nickel manganites by co-precipitation method." *Materials Science for Energy Technologies* 3 (2020): 201-208.

[37] Sivakumar, Thirumuruganantham, Radhakrishnan Anbarasan, Jeyaperumal Kalyana Sundar, and Muppudathi Anna Lakshmi. "Enhancing the SHG effect of zinc chloride-doped DAST single crystals: new potential materials for nonlinear optical device applications." *Journal of Materials Science: Materials in Electronics* 31, no. 15 (2020): 12943-12954.

[38] Skaistys, E., and V. I. Sugakov. "The free-carrier absorption in polycrystals." *physica status solidi (b)* 48, no. 2 (1971): K99-K101.

[39] Alharbi, S. R., and A. F. Qasrawi. "Effects of Ge substrate on the structural and optical conductivity parameters of Bi2O3 thin films." *Optik* 181 (2019): 714-720.

[40] Madelung, Otfried. Semiconductors: data handbook. *Springer Science & Business Media,* 2004.

[41] Nakashima, Hiroshi, Keisuke Yamamoto, and Dong Wang. "development of metal source/drain Ge-CMOS using TiN/Ge and HfGe/Ge contacts." *ECS Transactions* 58, no. 9 (2013): 167.

[42] Khusayfan, Najla M., A. F. Qasrawi, Seham R. Alharbi, Hazem K. Khanfar, and T. S. Kayed. "Band offsets, dielectric dispersion and some applications of CdSe/GeO2 heterojunctions." *Optik* 231 (2021): 166506..

[43] Wang, Li, Jing-Jing Li, Qi Fan, Zheng-Feng Huang, Ying-Chun Lu, Chao Xie, Chun-Yan Wu, and Lin-Bao Luo. "A high-performance near-infrared light photovoltaic detector based on a multilayered PtSe 2/Ge heterojunction." *Journal of Materials Chemistry C* 7, no. 17 (2019): 5019-5027.

[44] Rehman, Sajid Ur, Faheem K. Butt, Fateh Hayat, Bakhtiar Ul Haq, Zeeshan Tariq, F. Aleem, and Chuanbo Li. "An insight into a novel cubic phase SnSe for prospective applications in optoelectronics and clean energy devices." *Journal of Alloys and Compounds* 733 (2018): 22-32.

[45] Gilbert, L. R., R. Messier, and R. Roy. "Black germanium solar selective absorber surfaces." *Thin Solid Films* 54, no. 2 (1978): 149-157.

[46] Stepanov, A. L., and A. M. Rogov. "Optical reflectance of germanium surface modified by implanted silver ions." *Optics Communications* 474 (2020): 126052.

[47] Al Garni, S. E., and A. F. Qasrawi. "Exploring the optical dynamics in the ITO/As2Se3 interfaces." *Journal of Electronic Materials* 48, no. 10 (2019): 6319-6326.

[48] Seeger, Karlheinz. *Semiconductor physics*. Springer Science & Business Media, 2013.

[49] Dayo, A., and J. Krim. "Atomic-scale friction in Xe/Ag and N2/Pb." *International journal of thermophysics* 19, no. 3 (1998): 827-834.

[50] Daly, C., and J. Krim. "Sliding friction of solid xenon monolayers and bilayers on Ag (111)." *Physical review letters* 76, no. 5 (1996): 803.

[51] Shenvi, Neil, Hongzhi Cheng, and John C. Tully. "Nonadiabatic dynamics near metal surfaces: Decoupling quantum equations of motion in the wide-band limit." *Physical Review A* 74, no. 6 (2006): 062902.

[52] Khusayfan, Najla, Hazem K. Khanfar, and Sabah E. AlGarni. "Optical dynamics at the MoO3/ZnPc interfaces prepared for visible light communications." *Physica Scripta* 95, no. 7 (2020): 075503.

الملخص

الخصائص البنائيه والضوئية لرقائق الكادميوم برومايد الناميه على قواعد الجيرمانيوم

في هذه الأطروحة ، يتم طلاء $CdBr_2$ الرقيق على ركائز من الزجاج الرقيق وغير متبلورة من نوع Ge. تتميز طبقات ثنائية $Ge / CdBr_2$ المشيدة من الناحية الهيكلية والبصرية. أظهر تحليل حيود الأشعة السينية أن أغشية Ge و $CdBr_2$ و $Ge / CdBr_2$ التي نمت بتقنيات التبخر الحراري هي عبارة عن هياكل غير متبلورة ومتعددة البلورات ، على التوالي. أدى طلاء $CdBr_2$ على Ge إلى زيادة في معلمات الشبكة ، والإجهاد الدقيق ، وأخطاء التراص ، وكثافة العيوب. بصريًا ، لوحظ انزياح أحمر ملحوظ في أطياف النفاذية والانعكاس عند طلاء $CdBr_2$ على Ge. زادت قابلية امتصاص الضوء في نطاقات الضوء المرئية والأشعة تحت الحمراء بأكثر من 80 مرة مما يسمح بامتصاص الضوء على نطاق واسع. ويلاحظ أيضًا أن فجوة نطاق الطاقة قد انزاحت إلى الأحمر من 3.32 إلى 3.27 فولت نتيجة لاستبدال الزجاج بركائز Ge غير متبلورة. من ناحية أخرى ، اتبعت أطياف العزل الكهربائي لـ $Ge / CdBr_2$ في الغالب تلك الخاصة بـ Ge مما يعني أن قيم ثابت العزل قد زادت بشكل كبير. بالإضافة إلى ذلك ، فإن استخدام نموذج Drude - Lorentz لتحديد معلمات التوصيل البصري قد أظهر أنه يمكن زيادة حركة الانجراف وتردد الطحين لـ $CdBr_2$ عند استبدال الزجاج بـ Ge. زاد تردد مأكل الطحين بشكل ملحوظ ووصل إلى قيم 12 جيجاهرتز مما يجعل واجهات $Ge / CdBr_2$ واعدة للتطبيق في تكنولوجيا الاتصالات.